Volume 1 | Number 1 | Jan 2013 | Pages 1–100

Journal of
Materials Chemistry A

Materials for energy and sustainability
www.rsc.org/materialsA

ROYAL SOCIETY
OF CHEMISTRY

ROYAL SOCIETY
OF CHEMISTRY

www.rsc.org/materialsA

2D covalent triazine framework: a new class of organic photocatalyst for water splitting

Xue Jiang [1], Peng Wang [1], Jijun Zhao [1,2,3*]

[1] *Key Laboratory of Materials Modification by Laser, Ion and Electron Beams (Dalian University of Technology), Ministry of Education, Dalian 116024, China*

[2] *Beijing Computational Science Research Center, Beijing 100089, China*

[3] *Yangzhou Institute of Energy and Material, Chinese Academy of Sciences, Yangzhou 225127, China*

Abstract

Since the graphene boom, great efforts have been devoted to the two-dimensional (2D) monolayer materials with exciting perspectives of applications. Most known 2D materials so far are inorganic. Using the covalent triazine framework (CTF) as a representative, here we explore 2D organic semiconductors using first-principles calculations. From a systematic study of the electronic band structures, work functions, CBM/VBM positions, and optical absorption spectra, we identified the CTF as a new class of 2D visible-light-driven organocatalyst for water splitting. Controllable construction of such CTF from suitable organic subunit paves a way to correlate band alignment and chemical composite. In addition, multilayer CTFs have enhanced visible-light absorption compared to the monolayer ones due to interlayer coupling. Our theoretical prediction not only has fulfilled the organic counterparts of inorganic photocatalyst for water splitting, but also would motivate scientists to further search novel 2D organic materials with other technological applications.

* Corresponding author. Email: zhaojj@dlut.edu.cn (J. Zhao)

1. INTRODUCTION

The depletion of fossil fuels and the serious environmental problems with their combustion urge us to search for alternative sources of sustainable, cheap, and clean energy. One of such promising energy carriers is hydrogen. Hydrogen production via photocatalytic water splitting under visible-light irradiation offers a viable strategy for solving both problems simultaneously; but there are still many material-related issues that hinder its widespread usage [1, 2]. It is particularly difficult to search an efficient, simple, and highly active semiconductor material that satisfies all the crucial requirements: (i) the ideal band gap should be around 2.0 eV for effective utilization of the maximum portion of the solar visible light; (ii) the water oxidation (H_2O/O_2) and reduction (H^+/H_2) potentials must lie between conduction band minimum (CBM) and valence band maximum (VBM); (iii) the energy difference between VBM (CBM) and water oxidation (reduction) potential should be sufficiently large to ensure strong oxidizing (reducing) power; (iv) the surface area, porosity or reactive facets should be large enough for high activities [3-6]. In addition to all these issues, a photocatalyst still has to overcome the recombination of photoinduced charge carriers [1, 2].

To fulfill the above criteria, a fantastic choice is the two-dimensional (2D) materials, which have been proven as promising photocatalysts for pure water under UV irradiation. The nature of low dimensionality means that they have limited thickness, attractive and tunable electronic properties, and large surface area compared to the traditional bulk materials. In addition, monolayer materials minimize the migration distance for the generated electrons and holes, thus reducing the possibility of electron-hole recombination [7]. To date, the photocatalytic activities of several kinds of 2D materials [7-19] have been explored and these materials have been further chemically modified to improve their performance.

Currently, most 2D semiconductor materials are inorganic [7-19], including transition metal dichalcogenides [8-12], group-III monochalcogenide [7], graphene oxide (GO) [13-15] and GO-based composites [16-19]. In contrast to the extensive element-to-element search of inorganic 2D candidate materials on the periodic table, organocatalysts have not been well investigated yet. Note that many conventional inorganic materials and devices have now found their organic counterparts, such as organic superconductors [20], organic light-emitting diodes (OLED) [21], organic solar cells [22], organic field effect transistors [23], organic topological insulator [24, 25]. Usually, organic counterparts of inorganic materials have advantages of low cost, easy fabrication and mechanical flexibility. In particular, organic photocatalysts are able to overcome the weaknesses of their inorganic counterparts, i.e., limited concentration of active sites [26] and heavy metal with perceptive toxicity [27]. Therefore, a critical question is: whether an organocatalysts for water splitting exist among the broad range of possible organic materials?

Recent advances on synthetic chemistry and nanotechnology have shown great potential in fabricating very complex 2D organic lattices. Among them, two-dimensional covalent triazine frameworks (2D-CTFs) constitute a special and emerging class of covalent organic framework (COF), which are synthesized by trimerization reaction of carbonitriles and adopted triazine ring ($C_3N_3H_3$) as the building units [28-30]. 2D-CTF materials usually exhibit a regular architecture and periodic pore structure, showing crystalline feature. From the synthetic and theoretical points of view, 2D-CTF materials are attractive owing to their flexible parameters, i.e., controllable C/N/H composition, surface area and pore size. Moreover, 2D-CTF organic materials could be possible candidates for organocatalysts due to the following two reasons. Firstly, the 2D-CTF is structurally and chemically analogous

to g-C$_3$N$_4$, which is constructed by the same organic subunits of triazine ring. The discovery of g-C$_3$N$_4$ as a very promising metal-free photocatalyst can be traced back to 2006 [6]. Recently many strategies, such as heteroatom doping [5, 31], multilayer stacking [27, 32], metal cocatalysts [33], and adsorbed dyes [34], have been proposed to enhance its photocatalytic properties. Secondly, 2D-CTFs have tunable porosity, which may contribute to the enhancement of photoconversion efficiency in the visible range. Wang and coworkers [35] found that the efficiency of hydrogen production from the photochemical reduction of water by introducing mesoporosity into g-C$_3$N$_4$ could be improved by 8.3 times, which were conformed to be even higher than the commercial nitrogen-doped TiO$_2$ [36].

Here we aim to unveil whether or not 2D-CTFs are suitable for visible-light-driven photocatalysts using first-principles calculations. Some key physical properties that determine photocatalytic activity, including the electronic band structure, work function, CBM/VBM position, and optical absorption spectra, are obtained for 2D-CTFs. We demonstrate that the light harvesting capability of 2D-CTFs can be enhanced via tailoring the number of layers and pore size. The correlation between band alignment and chemical composition as well as geometry parameters of CTFs is discussed, which provides vital insight for designing optimal photocatalyst and bringing out new opportunities for other 2D organic materials.

2. COMPUTATIONAL METHODS

Within density functional theory (DFT), first-principles calculations were carried out using the Vienna ab initio simulation package (VASP) [37]. 2D-CTFs were simulated by slab models with a vacuum thickness of 15 Å, which is sufficient to isolate the adjacent sheets. The Brillouin zone integrations were performed using Γ-centered **k**

point meshes with uniform spacing of 0.026 Å^{-1}. The exchange-correlation interaction was treated by the generalized gradient approximation (GGA) using the Perdew-Burke-Ernzerhof (GGA-PBE) exchange-correlation functional [38]. We employed the projected augmented wave (PAW) method [39] and an energy cutoff of 800 eV to describe the electron wave function. In all calculations, self-consistency was achieved with a tolerance in the total energy of at least 0.01 meV. For the monolayer 2D-CTF systems, a more accurate Heyd-Scuseria-Ernzershof (HSE) screened potential method [40] was used to calculate the band gap. Van der Waals correction of the Grimme's D2 scheme [41] was also incorporated to better describe the non-covalent interaction for multilayer CTFs.

As a conventional method, the work function can be calculated by: $\varphi = V(\infty) - E_F$, where $V(\infty)$ and E_F are the electrostatic potential in a vacuum region far from the neutral surface and the Fermi energy of the neutral surface system, respectively [42]. The vacuum level was taken as the reference in the calculations of band alignment (VBM and CBM). Using the Kramers-Kroning dispersion relation [43], optical absorption spectra of the 2D-CTFs were computed from the imaginary part of dielectric function. Moreover, an ab initio molecular dynamics (AIMD) simulations have implemented to analyze to stability of the CTF structures under room temperature, the common procedure in AIMD following the method of Viñes et al. [44]. The initial configuration was given by the experimentally characterized structures and then left free to relax. After an initial quenching procedure where the system was heated up to 300 K. Later, a stabilization NVT run of 10 ps until energy is maintained using the Nosé thermostat, followed by a final NVE run of 10 ps. Overall, the time step 1 fs and the total AIMD runs were 30 ps.

3. RESULTS AND DISCUSSION

Three 2D-CTF models considered here come from the experimentally characterized structures, namely CTF-0 [28], CTF-1 [29], and CTF-2 [30], as shown in Figure 1a. The computed lattice constants for 2D hexagonal lattices are 7.25 Å (CFT-0), 14.57 Å (CFT-1), and 18.37 Å (CFT-2), respectively, in excellent agreement with the experimental values (7.3 Å, 14.57 Å, and 18.36 Å) [28-30]. In each unit cell, there are 15, 42, 60 atoms for CTF-0, CTF-1, CTF-2, respectively, and the ratio of N atoms decreases with cell size, i.e., 20% for CTF-0, 14.3% for CTF-1, and 10% for CTF-2, respectively. All these 2D-CTFs belong to porous configurations with pore radius of 5.604 Å (CTF-0), 14.018 Å (CTF-1), and 18.473 Å (CTF-2), respectively, which are larger than that of g-C_3N_4 (4.128 Å). Accordingly, the specific surface areas of these 2D-CTFs (3854 m^2/g for CTF-0, 4739 m^2/g for CTF-1, 4939 m^2/g for CTF-2) are larger than the theoretical limit of perfect g-C_3N_4 (2659 m^2/g) as well as the experimental value of mpg-C_3N_4 with defects (67-373 m^2/g) [35]. As pore size further increases, the surface area of 2D-CTFs would further increase. Therefore, these 2D-CTFs with tunable nitrogen concentration, porous configuration, and high surface area are expected to find promising applications as organic photocatalyst, as long as their electronic band structures match the aforementioned criteria.

To be a reliable photocatalyst, the monolayer CTFs have to be stable first. Previously, the stability of 2D-CTFs in an aqueous environment was reported, i.e., they are completely inert with respect to water [30]. Here, the stability of monolayer CTFs under room temperature in vacuum was examined by *ab initio* molecular dynamic (AIMD) simulation. We found that all these 2D covalent triazine frameworks remain stable at room temperature (T=300 K) after AIMD simulation. Their final snapshots are plotted in Figure 1b. During the simulation, the drops of total energy

and temperature are very small. For example, the average energy and temperature drop are just 0.08 meV/atom and 0.2 K per ps with standard deviations due to the ligand moieties of ± 0.009 eV and ± 0.013 K, respectively. One can see that all the structures of CTF-0, CTF-1, and CTF-2 under room temperature are slightly out-of-plane, especially the H atoms. To examine the behavior of torsion of the ligand moieties, we have calculated the torsion angles of eight random snapshots of AIMD for CTF systems and correlate them with their energy. We found that the larger is the pore size, the more is the degree of the torsion of the ligand moieties. For example, the average torsion angle is 1.23°, 1.42°, and 2.00° for CTF-0, CTF-1, and CTF-2, respectively. Further investigations on the energy difference between the perfectly planar structure and some snapshots of AIMD with different torsion angles confirm that the planar one is more stable at 0 K. Therefore, we concluded that these 2D organic sheets can be stable at room temperature either in vacuum or in aqueous environment.

Based on these stable configurations, we elucidate whether these 2D covalent triazine frameworks are suitable as photocatalyst for water splitting in terms of their electronic structures. Taking CTF-0 as a starting point, the calculated band gap is 2.49 eV at PBE level. It is well known that the conventional PBE functional within GGA underestimates the band gap of a semiconductor. A more accurate HSE06 hybrid functional yields a band gap of 3.32 eV for CTF-0 is (Figure 2a). In the 2D Brillouin zone, both CBM and VBM locate at K point, corresponding to a direct band gap. Although the HSE06 band gap of CTF-0 is 0.73 eV larger than the PBE value, it still falls in the marginal visible light region.

To gain more insight into the electronic structures of CTF-0 monolayer sheet, we plot the partial density of states (PDOS) in Figure 2b. Almost all conducting states in

the vicinity of the Fermi level originate from nitrogen atoms. In the triazine subunit of CTF-0, each nitrogen atom only bonds with two carbon atoms, leaving an unpaired electron plus a lone pair of electrons. This might accounts for the active sites of g-C_3N_4, as pointed out by Wang et al. [45] In short, N atoms in CTF-0 are crucial for its electronic properties and play a critical role in tuning the UV photocatalytic activity for direct water splitting.

The band edge alignment of CTF-0 calculated with HSE06 functional is presented in Figure 2c, which indicates that the CBM is 1.173 eV more negative than the reduction potential of H^+/H_2 and VBM is 0.917 eV more positive than the oxidation level of O_2/H_2O. As a consequence, the hole at the HOMO is sufficiently reactive to oxidize water to oxygen, while the electron at the LUMO has enough reduction potential to reduce water to hydrogen.

We also simulated the optical absorption spectra of CTF-0 to further examine whether they meet the criteria for efficient visible-light absorption. Figure 2d clearly shows that CTF-0 is able to harvest the visible light. Although CTF-0 has semiconductor characteristic, suitable band edge position and the ability of visible light absorption, there are still some practical issues related to the efficiency of solar energy conversion. Most of all, the band gap is somehow too large to absorb a significant fraction in the visible light region, leading to a rather low photoconversion efficiency. Therefore, the remaining question is how to achieve more suitable photovoltaic CTF-based materials by reducing the band gap.

According to the above analysis of PDOS, tailoring the nitrogen content of CTFs seems to be a possible way to enhance the solar conversion efficiency. In fact, previous experiments have already demonstrated the effect of N doping in carbon-based photocatalysts [46-51]. Incorporation of N atoms in monolayer graphene

modifies two key properties that are related to the efficiency of photocatalyst: work function and electronic band structure. Luo et al. [46] reported that nitrogen dopants lower the work function of graphitic carbon materials by enhancing the electron density. It was also found that incorporation of nitrogen can dramatically alter the electronic band structures [50, 51], e.g., resulting in metal-semiconductor transition of graphene [47]. In addition, Malko et al. [52] have shown that the band gap of graphynes containing boron and nitride heteroatoms are different from with a 2D all-carbon graphene (6_{BN}, 6, 12 graphyne), which exhibits a band gap due to missing reflection symmetry. More excitingly, some N-doped carbon nanomaterials were found to be excellent metal-free catalysts for oxygen reduction [48, 49].

All these findings motivate us to search other covalent triazine frameworks with better performance as organocatalyst. As mentioned above, CTF-1 and CTF-2 have the same triazine subunit as CTF-0 but different pore sizes. The corresponding N contents are 14.3% and 10%, respectively, both are less than 20% of CTF-0. Hence, it would be crucial to explore their photocatalytic performance and to elucidate the effect of nitrogen concentration.

Our PBE calculations show that all these 2D-CTFs are semiconductors with direct gaps, i.e., 2.49 eV for CTF-0, 2.42 eV for CTF-1, and 2.07 eV for CTF-2, respectively. Such reduction trends indicates that the band gap is affected by the nitrogen concentration. But this effect is also mixed with the pore size effect simultaneously. In order to distinguish the two effects, we build two classes of equivalent structures of 2D-CTFs with or without triazine units (C_3N_3), namely CTF-0a, CTF-1a, CTF-0b, and CTF-1b, which are shown in the Figure 3. They have the same pore size with CTF-0 and CTF-1, respectively. The N content are 50% for CTF-0a and 11% for CTF-1a, which is higher than the 20% for CTF-0 and lower than

14.3% for CTF-1. Obviously, we have ruled out the effect of adding N atom as considering the CTF-0b and CTF-1b. The computed band gap are 0.9 eV for CTF-0a, 2.53 eV for CTF-1a, 2.59 eV for CTF-0b, and 3.23 eV for CTF-1b, respectively. Comparison of CTF-0, CTF-0a, and CTF-0b (as well as CTF-1, CTF-1a and CTF-1b) demonstrates that band gap decreases with the increasing N content. Hence, we speculate that the band gap will overcome 2 eV as N content are about 30%, 5% and 8% for CTF-0, CTF-1, and CTF-2, respectively. Too much or too little N doping is detrimental for band gap engineering. In view of the fact that the band gap decreases from 2.49 eV to 2.42 eV to 2.07 eV for CTF-1, CTF-2, and CTF-3 as the N content decreases, this opposite N concentration effect reveals a competing pore size effect, that is, smaller pore size induces a larger band gap.

To get more insight into the variation of electronic structures due to incorporation of nitrogen, the partial charge density distribution for the edges of valence and conduction bands of CTF-0 and CTF-0a are presented in Figure 4, respectively. For the CTF-0, charge distribution on the VBM and CBM are mainly localized at the p_x and p_y orbitals of nitrogen atoms and the p_z orbitals of carbon and nitrogen atoms. As the nitrogen concentration rises to 50%, the number of unpaired electrons and lone pair of electrons increase. As a consequence, the charge distributions of the edges of valence and conduction bands of CTF-0a show more delocalized electrons on the p_x and p_y orbitals of nitrogen and carbon atoms, resulting in a shrinkage of band gap.

On the other hand, the underlying mechanism of pore size effect can be attributed to the quantum confinement effect. As displayed in Figure 1, every six, twelve, and eighteen C_3N_3/C_6 rings enclose a pore in the CTF-0, CTF-1, and CTF-2 network, respectively. Coupling of more six-membered rings tend to reduce the band

gap. By addition of cycles, the π electrons become more and more delocalized, and this is responsible of the band gap reduction. For example, Riga et al. [53] observed the band gap of benzene, naphthalene, anthracene, and tetracene are 7.8 eV, 5.4 eV, 3.9 eV, and 3.0 eV by E. S. C. A. valence band spectra, respectively. The tunable band gaps of graphynes and other ordered macroporous materials containing pores of different sizes have also been observed by Malko et al. [52, 54] and Imhof et al. [55]. Very recently, Martin et al. [56] demonstrated by experimental analysis that pore size effect can further enhance quantum yield of g-C_3N_4 in the visible region to 26.5%, which is nearly an order of magnitude higher than that for any other existing g-C_3N_4 photocatalysts.

To compare the reducing and oxidizing power for CTF-0, CTF-1, and CTF-2, we align their band positions (calculated with PBE functional) in Figure 5. Clearly, both CTF-1 and CTF-2 are able to produce H_2 and O_2 as photocatalysts. Compare to CTF-0, the VBM positions of CTF-1 and CTF-2 shift upward by 0.098 eV and 0.662 eV, respectively, while the conduction band edge moves to higher energy range by 0.038 eV and 0.242 eV, respectively. Generally speaking, the photocatalytic efficiency depends on the numbers of electrons/holes having higher potential than the water reduction/oxidation potential. The larger difference, the higher the reducing/oxidizing power. Therefore, the upwards shift of absolute band positions from CTF-0 to CTF-1 and CTF-2 means that the reducing capability is strengthened but the oxidizing capability is weakened with decreasing nitrogen concentration. In other words, the larger energy difference between VBM and oxidation potential (O_2/H_2O) of CTF-0 is better for the water oxidation among three CTF models explored; whereas the larger energy difference between CBM and reduction potential (H^+/H_2) of CTF-2 is more favorable for hydrogen production. The shifts of CBM and VBM together give rise to

the decreased effective band gap to 2.42 eV for CTF-1 and 2.07 eV for CTF-2, which is beneficial for more efficient solar energy conversion. As stated above, the decrease of nitrogen content in CTFs would result in significant narrowing of band gap and thus enhanced capability to reduce water into H_2, in good agreement with previous finding for N-doped graphene [46, 47]. According to the principle of reticular chemistry, it is well known that the topology of frameworks and the corresponding physical/chemical properties are imposed by the geometrical features of the building blocks and linking modes [57]. Therefore, by further optimizing the secondary subunits and linkers via a more complete search in the future, organic molecular architectures with suitable work function and electronic band structure (and thus high efficient visible-light absorption) can be designed and constructed in experiments by self-condensation and co-condensation of chosen monomers for practical applications.

According to the powder X-ray diffraction (PXRD) patterns [28-30], the bulk CTF-0, CTF-1, and CTF-2 have eclipsed or staggered structures stacked with interlayer van der Waals force. The fundamental electronic properties such as band gap and work function might be further tuned by stacking of 2D-CTFs, similar to the graphitic carbon nitrides [32, 58]. Here we considered multilayer CTF-0 (layer number: N=1~6) with AA eclipsed stacking, since AA face-to-face stacking maximizes π-orbital overlap that is the most favorable for charge transport [59] and improvement of the photodecomposition reaction. As the number of CTF-0 layers increases to six, the total number of atoms in supercell and the largest lattice constant reach 90 and 45 Å, respectively. It is therefore too computationally expensive to perform geometry optimizations and electronic structure calculations at the HSE06 level. Alternatively, we adopted the PBE method to describe the shift of band edge positions and band gap of multilayer CTF-0. As a well-known deficiency, PBE functional usually

systematically underestimates the band gap. Moreover, the detailed band alignment might be also different from the HSE06 results. For example, the energy differences between CBM (VBM) and reduction (oxdation) potential are 1.173 eV (0.917 eV) and 0.578 eV (0.682 eV) from HSE06 and PBE calculations, respectively. However, we found that the choice of method does not affect the redox activities of CTFs. Both sets of values indicate that CTF could be a new class of 2D visible-light-driven organocatalyst for water splitting. Moreover, the general trends for variation of band gap and shift of band edge positions from our PBE calculations would be still valid. Note again that our main discussions here are based on the results from PBE calculations. Although HSE06 is a priori show in the same situation, similar trends are supposed to be deduced from the HSE06 calculations.

The electronic band gaps and work functions for multilayer CTF-0 are listed in Table 1. Overall speaking, the band gap reduces with increasing number of layers monotonically, while the work function is insensitive. All multilayer CTF-0 are still direct gap semiconductor. At PBE level, their effective band gaps are 2.36, 2.32, 2.30, 2.29, and 2.28 eV for systems with two-, three-, four-, five-, and six-layers, respectively, compared to 2.49 eV for the monolayer one. Also note that the band gap of multilayer CTF-0 already converges to the bulk limit of 2.28 eV when the number of layers reaches six. In short, the magnitude of band gap variation is 0.21 eV (at PBE level) by stacking up to six layers of CTF-0 sheets.

The change of band gap can be attributed to the interlayer coupling of valence electrons. To understand this mechanism, Figure 6 plots the charge density difference of a bilayer CTF-0, which are constructed by subtracting the integrated electron density of the bilayer CTF-0 from the summation of two individual CTF-0 monolayers. One can clearly see redistribution of the charge density by forming the

triangular-shaped electron rich regions above the triazine ring. Such charge redistribution drives the inhomogeneous intra-layer charge transfer within CTF-0 plane. As a consequence, the strength of intra-layer C-N and C-H bonds is significantly reduced, and the N-N coupling between two adjacent layers is strengthened, which partially saturates the nonbonding electrons from the nitrogen atoms.

To evaluate the photocatalytic capability of multilayer CTF-0s further, we align the energy levels of multilayer CTFs with respect to the water oxidation/reduction potential levels in Figure 7. In the case of bilayer system, the VBM shifts upward by 0.088 eV and CBM moves downward by 0.043 eV with regard to the monolayer one. For the other multilayer CTF-0 systems, the VBM is almost invariant, whereas the CBM moves towards the higher energy region by 0.3~0.5 eV. For multilayer CTF-0, both redox reactions are thermodynamically possible with good reaction rates, since the VBM is deep enough with respect to the water oxidation potential and the CBM also locates at a satisfactory position with respect to the water reduction potential level.

To further clarify the interlayer coupling effect on the 2D-CTFs and extend this universal strategy to other 2D organic systems, we also considered the case of multilayer CTFs with AB stacking. First of all, our energy calculations show that the energies of AB stacking are lower than AA stacking about 0.02 eV per CTF-0 layer. Secondly, the reduction of the band gap via stacking on AB seems to be slightly lower (0.1 eV) than on AA as shown in Figure 7. The small band gap difference of AB and AA stacking is determined by the electronic repulsive perturbation and interlayer coupling induced charge transport. On the one hand, higher electronic repulsive perturbation of valence and conduction bands results in a larger band gap of AB

stacking than AA stacking. On the other hand, stronger π-orbital overlap of AA stacking is more favorable for charge transport between interlayer and intralayer, which will result in redistribution of the charge density. The latter seems to be more pronounced than the electronic repulsive perturbation for CTFs. More importantly, compared to the energy levels of AB and AA stacked CTFs, we can see that the different stacking modes yield nearly the same results. That is to say, stacking 2D-CTFs is an effective way to improve the flow of the carrier and reduce the band gap, which will enhance the optical absorption behavior in the visible light region. More important, our design strategy of taking advantage of the effects of pore size, nitrogen content and multilayer stacking is universal and will be helpful for exploring the other 2D organic photocatalytic materials in the future.

4. CONCLUSION

Using first-principle calculations, we have systematically studied the electronic structure, work function, optical properties, and band edge alignment for a series of monolayer and multilayer covalent triazine frameworks. Although the monolayer CTF-0 sheet has slightly large band gap to absorb a significant fraction in visible light region, the band gap of 2D-CTFs can be effectively reduced by three strategies, i.e., interlayer coupling, tuning of pore size and nitrogen content. The calculated band edge alignment further show better behavior of visible-light absorption. All these findings demonstrate that 2D-CTFs is a new family of organocatalysts materials for visible-light-drive water splitting. Our theoretical results are expected to stimulate experimentalists to further study novel 2D metal-free organic materials as visible-light photocatalyst, which combine the unique advantages of high surface area, low cost, chemically and thermally stable in aqueous, easy fabrication and mechanical

flexibility. More importantly, our strategies of designing and modifying 2D organic materials may further encourage scientists to search other unknown 2D organic materials in the future, which will broaden the scope and scientific impact of organic materials and devices.

Table 1. The work function (WF) and band gap (E_g) of two-, three-, four-, five-, and six-layer 2D CTF-0s computed with PBE functional. The band gap differences (ΔE_g) between the multilayers and monolayer CTF are shown in this Table.

N	1	2	3	4	5	6	∞
WF (eV)	6.35	6.26	6.35	6.34	6.34	6.35	--
E_g (eV)	2.49	2.36	2.32	2.30	2.29	2.28	2.28
ΔE_g (eV)	0	0.13	0.17	0.19	0.20	0.21	0.21
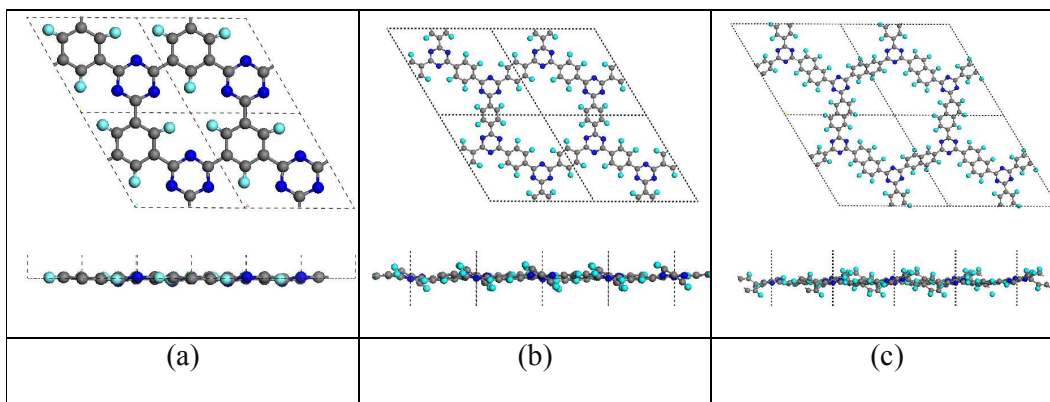
Figure 1. The snapshot images of the equilibrium structures of CTF-0 (a), CTF-1(b), and CTF-2 (c) at the end of AIMD simulation. The top one is the top view, and the bottom one is the side view. The grey, dark blue and light green atoms are C, N, and H, respectively.
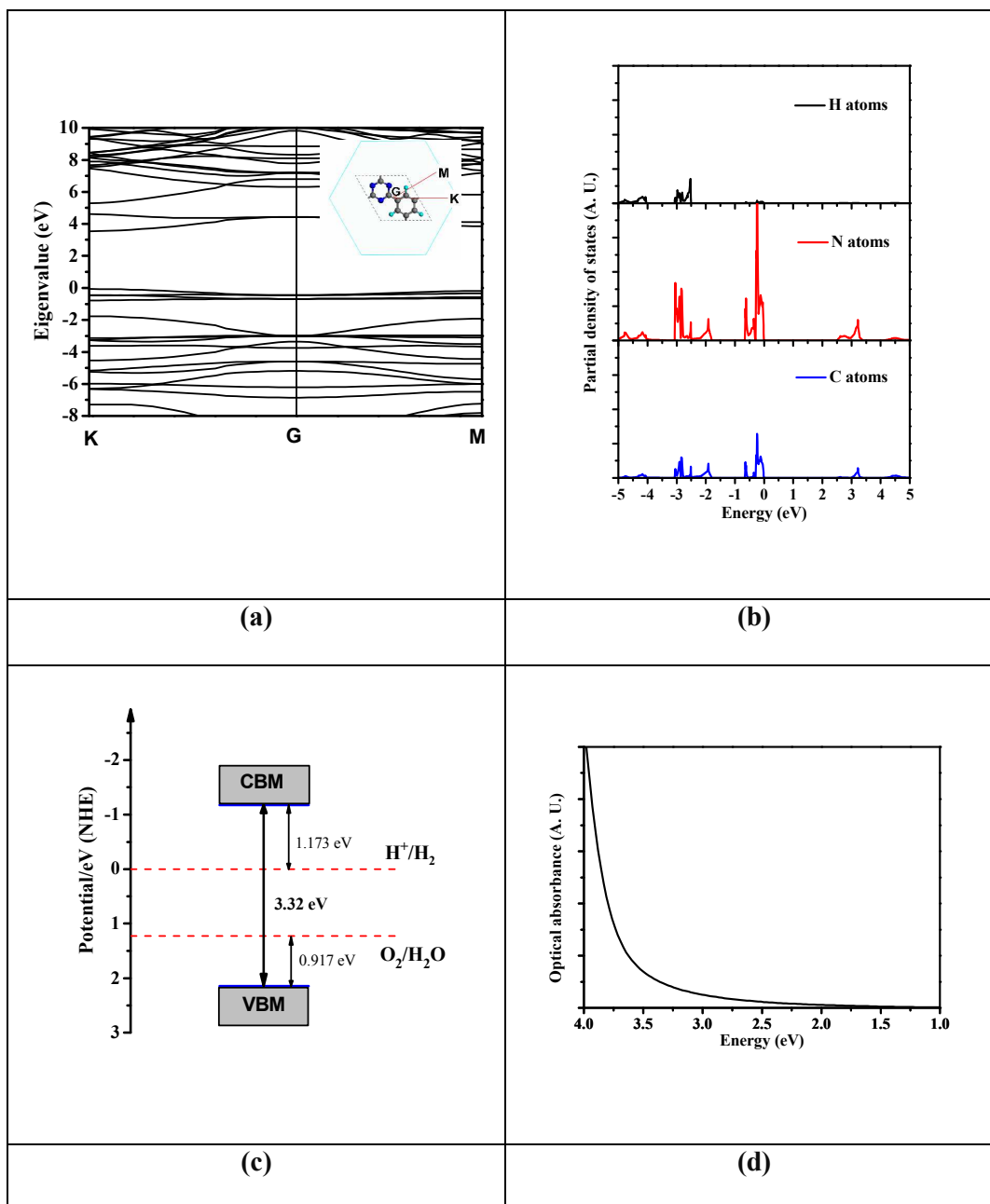
Figure 2. (a) Calculated band dispersion and (b) projected density of states of CTF-0 with HSE06 methods, the valence band maximum is set to zero. (c) Band alignments of CTF-0 with respect to the standard water redox potentials. (d) Optical absorption of CTF-0.
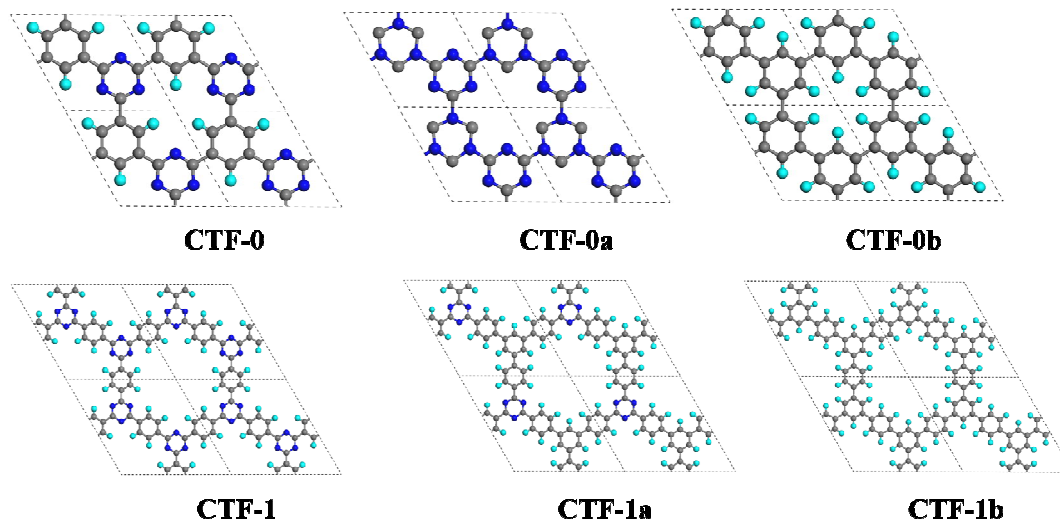
Figure 3. The equilibrium structures of CTF-0, CTF-0a, CTF-0b, CTF-1, CTF-1a, and CTF-1b. The grey, dark blue and light green atoms are C, N, and H, respectively.
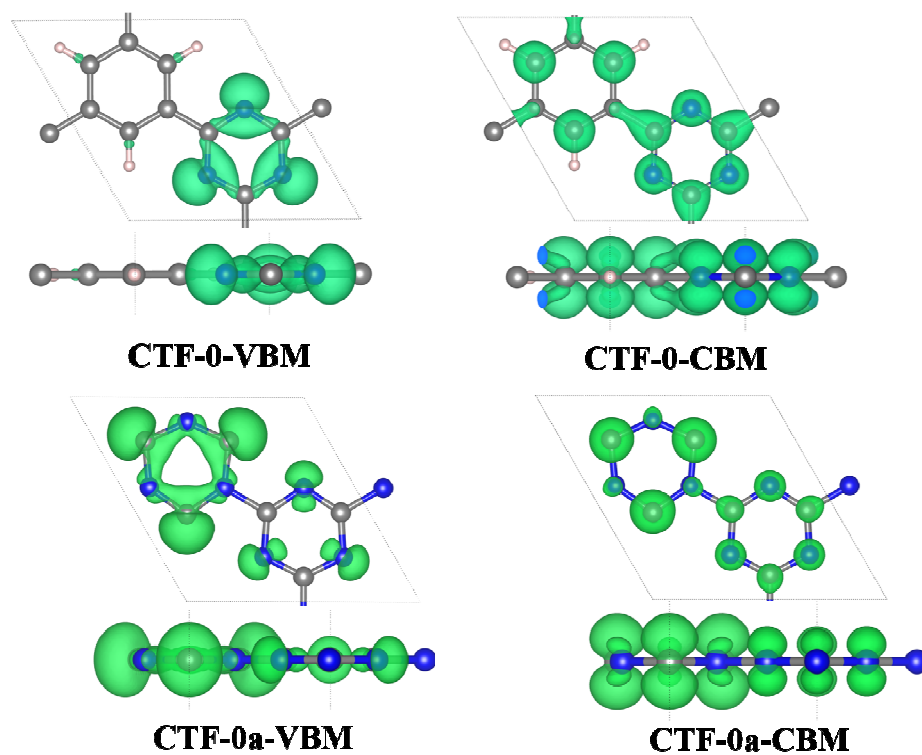
Figure 4. Charge density distribution of CBM and VBM state of CTF-0 and CTF-0a. The isosurface value is set to be 0.03 eÅ^{-3}. The grey, dark blue and pink atoms are C, N, and H, respectively.
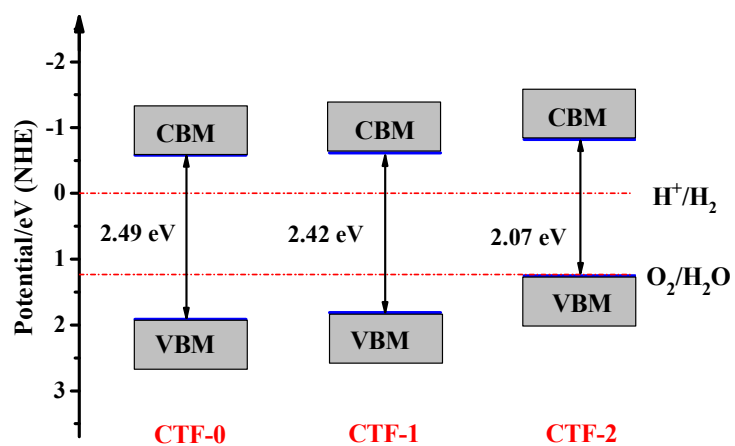
Figure 5. Band edge alignments of CTF-0, CTF-1, and CTF-2, respectively. The dot

lines are standard water redox potentials. The reference potential is the vacuum level.

Top view   Side view
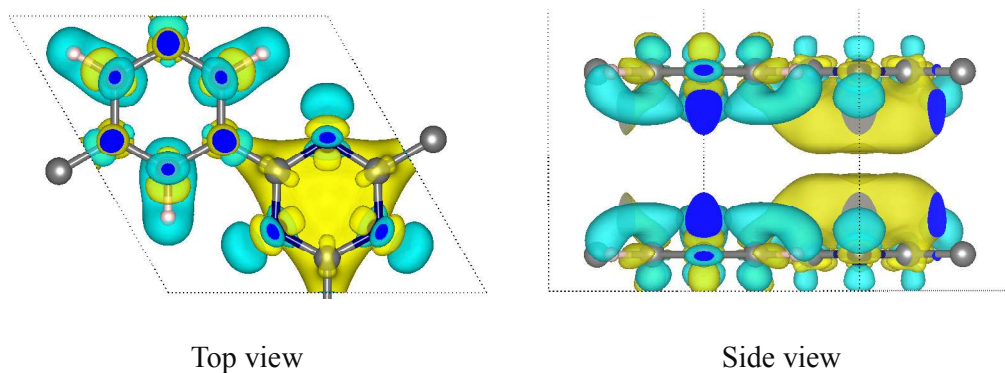
Figure 6. Charge density difference of a bilayer CTF-0. Yellow color shows the charge accumulated regions, and blue color shows the charge depleted regions. The grey, dark blue and pink atoms are C, N, and H, respectively.
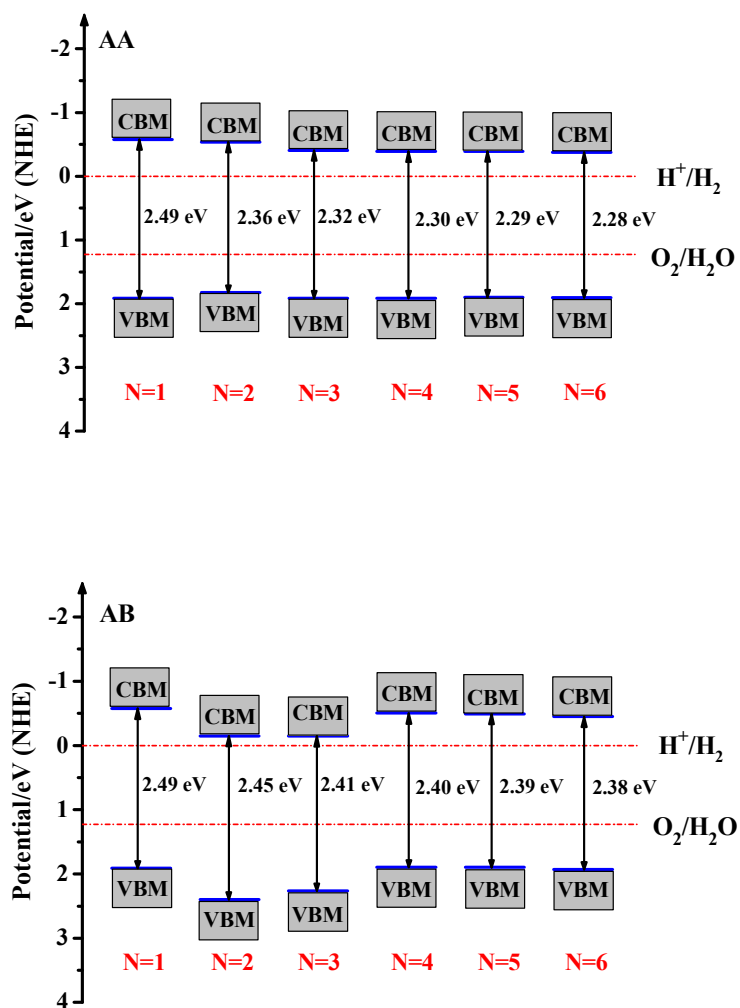
Figure 7. Band edge alignments of CTF-0 with AA stacking (upper) and AB stacking (bottom), respectively. The dot lines are standard water redox potentials. The reference potential is the vacuum level.

References

1.   M. R. Hoffmann, S. T. Martin, W. Choi and D. W. Bahnemann, *Chem. Rev.*, 1995, 95, 69-96.

2.   D. Chen, L. Tang and J. Li, *Chem. Soc. Rev.*, 2010, 39, 3157-3180.

3.   J. Yu, W. Wang, B. Cheng and B. L. Su, *J. Phys. Chem. C*, 2009, 113, 6743-6750.

4.   N. Wu, J. Wang, D. N. Tafen, H. Wang, J. G. Zheng, J. P. Lewis, X. Liu, S. S. Leonard and A. Manivannan, *J. Am. Chem. Soc.*, 2010, 132, 6679-6685.

5.   G. Liu, P. Niu, C. Sun, S. C. Smith, Z. Chen, G. Q. Lu and H. M. Cheng, *J. Am. Chem. Soc.*, 2010, 132, 11642-11648.

6.   X. Wang, K. Maeda, A. Thomas, K. Takanabe, G. Xin, J. M. Carlsson, K. Domen and M. Antonietti, *Nat. Mater.*, 2009, 8, 76-80.

7.   H. L. Zhuang and R. G. Hennig, *Chem. Mater.*, 2013, 25, 3232-3238.

8.   H. L. Zhuang and R. G. Hennig, *Phys. Rev. B*, 2013, 88, 115314.

9.   H. L. Zhuang and R. G. Hennig, *J. Phys. Chem. C*, 2013, 117, 20440-20445.

10. J. Kang, S. Tongay, J. Zhou, J. Li and J. Wu, *Appl. Phys. Lett.*, 2013, 102, 012101.

11. N. Singh, G. Jabbour and U. Schwingenschlögl, *Eur. Phys. J. B*, 2012, 85, 1-4.

12. Y. Li, Y. L. Li, C. M. Araujo, W. Luo and R. Ahuja, *Catal. Sci. Technol.*, 2013, 3, 2214-2220.

13. T. F. Yeh, C. Y. Teng, S. J. Chen and H. Teng, Adv. Mater., 2014, 26, 3297-3303.

14. X. Jiang, J. Nisar, B. Pathak, J. Zhao and R. Ahuja, *J. Catal.*, 2013, 299, 204-209.

15. T. F. Yeh, J. M. Syu, C. Cheng, T. H. Chang and H. Teng, *Adv. Funct. Mater.*, 2010, 20, 2255-2262.

16. Q. Li, B. Guo, J. Yu, J. Ran, B. Zhang, H. Yan and J. R. Gong, *J. Am. Chem. Soc.*, 2011, 133, 10878-10884.

17. J. Zhang, J. Yu, M. Jaroniec and J. R. Gong, *Nano Lett.*, 2012, 12, 4584-4589.

18. G. Xie, K. Zhang, B. Guo, Q. Liu, L. Fang and J. R. Gong, *Adv. Mater.*, 2013, 25, 3820-3839.

19. G. Xie, K. Zhang, H. Fang, B. Guo, R. Wang, H. Yan, L. Fang and J. R. Gong, *Chem–Asian J.*, 2013, 8, 2395-2400.

20. D. Jérome, A. Mazaud, M. Ribault and K. Bechgaard, *J. Physique Lett.*, 1980, 41, 95-98.

21. C. W. Tang and S. A. VanSlyke, *Appl. Phys. Lett.*, 1987, 51, 913-915.

22. D. Kearns and M. Calvin, *J. Chem. Phys.*, 1958, 29, 950-951.

23. H. Koezuka, A. Tsumura and T. Ando, *Synth. Met.*, 1987, 18, 699-704.

24. Z. F. Wang, Z. Liu and F. Liu, *Nat. Commun.*, 2013, 4, 1471.

25. Z. F. Wang, Z. Liu and F. Liu, *Phys. Rev. Lett.*, 2013, 110, 196801.

26. D. S. Su, J. Zhang, B. Frank, A. Thomas, X. Wang, J. Paraknowitsch and R. Schlögl, *ChemSusChem*, 2010, 3, 169-180.

27. X. Zhang, X. Xie, H. Wang, J. Zhang, B. Pan and Y. Xie, *J. Am. Chem. Soc.*, 2012, 135, 18-21.

28. P. Katekomol, J. Roeser, M. Bojdys, J. Weber and A. Thomas, *Chem. Mater.*, 2013, 25, 1542-1548.

29. P. Kuhn, M. Antonietti and A. Thomas, *Angew. Chem. Int. Edit.*, 2008, 47, 3450-3453.

30. M. J. Bojdys, J. Jeromenok, A. Thomas and M. Antonietti, *Adv. Mater.*, 2010, 22, 2202-2205.

31. J. Zhang, J. Sun, K. Maeda, K. Domen, P. Liu, M. Antonietti, X. Fu and X. Wang, *Energ.*

Environ. Sci., 2011, 4, 675-678.

32. F. Wu, Y. Liu, G. Yu, D. Shen, Y. Wang and E. Kan, *J. Phys. Chem. Lett.*, 2012, 3, 3330-3334.

33. K. Maeda, X. Wang, Y. Nishihara, D. Lu, M. Antonietti and K. Domen, *J. Phys. Chem. C*, 2009, 113, 4940-4947.

34. K. Takanabe, K. Kamata, X. Wang, M. Antonietti, J. Kubota and K. Domen, *Phys. Chem. Chem. Phys.*, 2010, 12, 13020-13025.

35. X. Wang, K. Maeda, X. Chen, K. Takanabe, K. Domen, Y. Hou, X. Fu and M. Antonietti, *J. Am. Chem. Soc.*, 2009, 131, 1680-1681.

36. S. C. Yan, Z. S. Li and Z. G. Zou, *Langmuir*, 2010, 26, 3894-3901.

37. G. Kresse and D. Joubert, *Phys. Rev. B*, 1999, 59, 1758-1775.

38. J. P. Perdew, J. A. Chevary, S. H. Vosko, K. A. Jackson, M. R. Pederson, D. J. Singh and C. Fiolhais, *Phys. Rev. B*, 1992, 46, 6671-6687.

39. P. E. Blöchl, *Phys. Rev. B*, 1994, 50, 17953-17979.

40. J. Heyd, G. E. Scuseria and M. Ernzerhof, *J. Chem. Phys.*, 2003, 118, 8207-8215.

41. S. Grimme, *J. Comput. Chem.*, 2006, 27, 1787-1799.

42. K. Seiji, N. Takashi and Y. Jun, *J. Phys. Confer. Ser.*, 2006, 29, 120.

43. M. Gajdoš, K. Hummer, G. Kresse, J. Furthmüller and F. Bechstedt, *Phys. Rev. B*, 2006, 73, 045112.

44. F. Viñes, J. Carrasco and S. T. Bromley, *Phys. Rev. B*, 2012, 85, 195425.

45. Y. Wang, X. Wang and M. Antonietti, *Angew. Chem. Int. Edit.*, 2012, 51, 68-89.

46. Z. Luo, S. Lim, Z. Tian, J. Shang, L. Lai, B. MacDonald, C. Fu, Z. Shen, T. Yu and J. Lin, *J. Mater. Chem.*, 2011, 21, 8038-8044.

47. D. Wei, Y. Liu, Y. Wang, H. Zhang, L. Huang and G. Yu, *Nano Lett.*, 2009, 9, 1752-1758.

48. K. Gong, F. Du, Z. Xia, M. Durstock and L. Dai, *Science*, 2009, 323, 760-764.

49. M. Lefèvre, E. Proietti, F. Jaouen and J. P. Dodelet, *Science*, 2009, 324, 71-74.

50. Q. Liu, B. Guo, Z. Rao, B. Zhang and J. R. Gong, *Nano Lett.*, 2013, 13, 2436-2441.

51. B. Guo, Q. Liu, E. Chen, H. Zhu, L. Fang and J. R. Gong, *Nano Lett.*, 2010, 10, 4975-4980.

52. D. Malko, C. Neiss and A. Görling, *Phys. Rev. B*, 2012, 86, 045443.

53. J. Riga, J. J. Pireaux, R. Caudano and J. J. Verbist, *Phys. Scr.*, 1977, 16, 346.

54. D. Malko, C. Neiss, F. Viñes and A. Görling, *Phys. Rev. Lett.*, 2012, 108, 086804.

55. A. Imhof and D. Pine, *Nature*, 1997, 389, 948-951.

56. D. J. Martin, K. Qiu, S. A. Shevlin, A. D. Handoko, X. Chen, Z. Guo and J. Tang, *Angew. Chem. Int. Edit.*, 2014, 53, 9240-9245.

57. D. Wu, F. Xu, B. Sun, R. Fu, H. He and K. Matyjaszewski, *Chem. Rev.*, 2012, 112, 3959-4015.

58. A. Du, S. Sanvito, Z. Li, D. Wang, Y. Jiao, T. Liao, Q. Sun, Y. H. Ng, Z. Zhu, R. Amal and S. C. Smith, *J. Am. Chem. Soc.*, 2012, 134, 4393-4397.

59. E. L. Spitler, B. T. Koo, J. L. Novotney, J. W. Colson, F. J. Uribe-Romo, G. D. Gutierrez, P. Clancy and W. R. Dichtel, *J. Am. Chem. Soc.*, 2011, 133, 19416-19421.